Progress In Electromagnetics Research M, Vol. 96, 33–43, 2020

Electromagnetic Loss Analysis and Temperature Field Estimate of Hybrid Double Stator Bearingless Switched Reluctance Motor

Yukun Sun[1, 2], Kai Cao[2], Ye Yuan[2, *], Shuaipo Guo[2], Niu Liu[3], and Le Li[3]

Abstract—A new hybrid double stator bearingless switched reluctance motor (HDSBSRM) realizes the decoupling of torque and suspension force from the structure, and the permanent magnet added in the inner stator further reduces the suspension power loss. For HDSBSRM, loss is the main cause of temperature rise. In order to ensure the stable suspension and rotation of the motor, loss of the Magnetic Bearing (MB) and motor are calculated and analyzed by finite element method (FEM). Based on the loss result, the temperature field is analyzed. The analysis of loss and temperature field provides important theoretical basis for the design of motor cooling system.

1. INTRODUCTION

Switched reluctance motor (SRM) has become one of the most popular motors because of its simple structure and excellent performance. However, the efficiency of SRM is not ideal because of its rotor salient structure and mechanical bearing loss at high speed. Therefore, magnetic bearing is used to replace the mechanical bearing to reduce the mechanical loss and increase the performance of SRM in the high-speed field. It has a broad application prospect in aerospace, flywheel battery, and other fields [1].

Bearingless switched reluctance motor (BSRM) combines a magnetic bearing system with the torque system of SRM and generates suspension force and torque to realize the suspension and rotate of the motor. Reference [2] put forward 12/8 double winding maglev SRM, and two sets of windings realized suspension and rotation, respectively, but two sets of windings increased the difficulty and cost of stator processing. Reference [3] put forward single winding maglev SRM, which reduced the system cost but increased the control difficulty. Reference [4] put forward double stator maglev SRM to realize the decoupling on the motor body, which basically solved the coupling effect of BSRM torque and suspension, greatly reducing the motor control difficulty. Based on this motor structure, permanent magnet was added to the inner stator to increase the radial suspension force of the motor in [5], which solved the problem of insufficient suspension force caused by the minimum suspension and reduces the suspension power loss of the motor.

In order to verify the performance of the motor, the finite element analysis is recognized as an effective tool [6–10]. Reference [11] realized the accurate modeling of BSRM by electromagnetic analytical method. Reference [12] studied the accurate calculation formula of iron loss of BSRM. Reference [13] calculated and analyzed the copper loss of SRM winding, providing the basis for the optimal design of motor winding. Reference [14], according to the non-linear characteristics of SRM, analyzed the transient temperature field of external rotor structure SRM. Reference [15] used the finite element method to solve the coupling of electromagnetic field and temperature field of motor and proposed LPTN model to make the thermal analysis method applicable to different structures and

Received 22 June 2020, Accepted 18 August 2020, Scheduled 31 August 2020

* Corresponding author: Ye Yuan (1763068656@qq.com).

[1] Jiangsu Collaborative Innovation Center for Smart Distribution Network, Nanjing 211167, China. [2] School of Electrical and Information Engineering, Jiangsu University, Zhenjiang 212013, China. [3] STATEGRID ZHENJIANG POWER SUPPLY COMPANY, Zhenjiang 212013, China.

parameters of motor. However, the calculation and analysis of HDSBSRM loss is more complicated compared with ordinary BSRM, and the analysis of its temperature field has not been covered in any literature.

This paper introduces the structure and operation principle of a 12/8/4 HDSBSRM and analyzes its loss and temperature characteristics. In the second section, the topological structure and operation mechanism of HDSBSRM are introduced. In the third section, the loss distribution of motor is analyzed by using calculation method and FEM respectively. Finally, the temperature field analysis model is established by using Workbench software; the heat dissipation coefficient of each part of motor is fully considered; and the temperature of HDSBSRM at 10000 rpm speed is analyzed. The analysis of loss and temperature field provides important theoretical basis for the design of motor cooling system.

2. STRUCTURE OF HDSBSRM

The structure diagram of HDSBSRM studied in this paper is shown in Fig. 1. The motor consists of an outer stator, a rotor, and an inner stator. The torque system consists of a rotor and an outer stator, and the suspension system consists of a rotor and an inner stator. The inner stator is divided into two independent suspension stators by the embedded permanent magnet in the middle of the inner stator, and the permanent magnet can reduce the power loss of the suspension winding and improve the operation efficiency of the motor. Four suspension poles are set at 90 degree interval between left and right inner stators, and each suspension pole has corresponding suspension winding to provide radial suspension force. The rotor and outer stator are similar to the ordinary 12/8 SRM. The rotor has a salient pole structure every 45 degrees, and there is no winding on the salient pole. The outer stator has a salient pole structure every 30 degrees, and a torque winding is on the salient pole. Four windings of 12 windings every 90 degrees are connected in series into the same phase, which is divided into three phases A, B, and C, controlled by three-phase asymmetric half bridge.

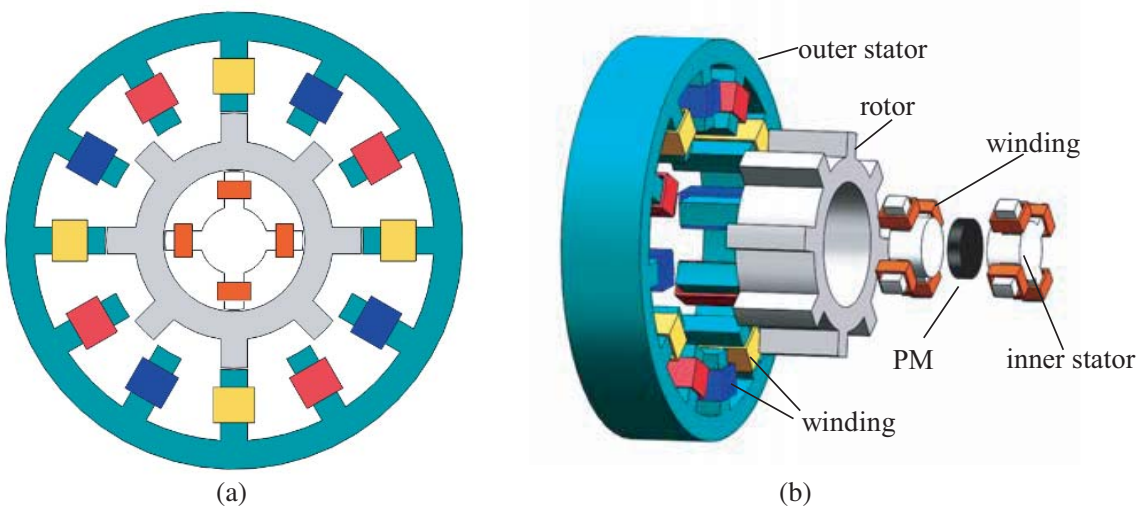

Figure 1. The structure of HDSBSRM. (a) Front view. (b) Exploded view.

The stator structure and magnetic circuit in HDSBSRM are shown in Fig. 2. When the rotor is in the balance position, there is no current in the suspension winding, and the permanent magnet generates bias flux. The bias flux density is the same in the positive and negative directions of XY, so the rotor can be in the balance position. When the rotor is eccentric, the displacement sensor inputs the displacement signal to the controller. The controller controls the main circuit to generate the control current for the suspension winding. The control current generates the control flux in the corresponding winding. After the control flux and the permanent magnet bias flux are superposed, the radial suspension force will be generated to pull the rotor back to the balance position. Table 1 lists the motor parameters studied in this paper.

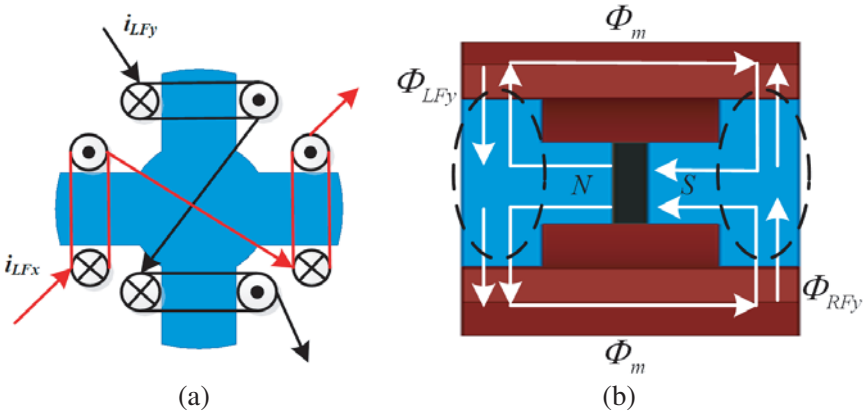

Figure 2. Inner stator structure and magnetic circuit. (a) Inner stator structure. (b) Magnetic circuit.

Table 1. Motor parameters.

Parameter	Value	Parameter	Value
Rated power P/W	1200	Rotor outer diameter D_r/mm	72
Rated speed n/rpm	10000	Rotor inner diameter D_i/mm	40
Rated efficiency η/%	80	Air gap g/mm	0.5
Rated voltage U/V	220	Magnetic block length L_1/mm	6.5
Outer Stator diameter D_s/mm	129	Rotor teeth Pole arc β_1/°	15
Permanent magnet diameter D_p/mm	19	Permanent magnet thickness L_2/mm	3.5
Rotor yoke height L_3/mm	8	Torque winding turns per phase N_1	40
Outer stator teeth Pole arc β_2/°	15	Suspension winding turns per phase N_2	60

3. LOSS ANALYSIS OF HDSBSRM

3.1. Loss Calculation Model

Efficiency is an important index to measure the performance of the motor. Accurate calculation of the loss is an important prerequisite to obtain the efficiency parameters of the motor. The complex structure of HDSBSRM makes the calculation of the loss extremely difficult. Generally, motor efficiency can be described as:

$$\eta = \frac{T_{av}\omega}{T_{av}\omega + P_{loss}} \tag{1}$$

where T_{av} is the average torque; ω is the angular velocity; P_{loss} is the total loss, which can be described as:

$$P_{loss} = P_{Cu} + P_{Fe} + P_s \tag{2}$$

where P_{Fe} is the iron loss; P_{Cu} is the copper loss; P_s is the additional loss; P_{Cu} includes the copper loss of inner stator winding and outer stator winding. When the motor is suspended stably by the permanent magnet bias magnetic field. The suspension current is 0 A, and the suspension winding loss is 0 W. Ignoring the skin effect, copper loss is directly proportional to the square of current:

$$P_{cu} = qI_m^2 R \tag{3}$$

where q is the phase number of motor; R is the winding resistance; I_m is the effective value of phase winding current. The calculation formula of each parameter can be described as follows:

$$\begin{cases} I_m = \sqrt{\dfrac{N_r}{2\pi}\displaystyle\int_{\theta_{off}}^{\theta_{on}} i^2(\theta)d\theta} \\ R_{=}\rho_{cu}\left(T_{cu}\right)\cdot\dfrac{2k_l L_{stk} N_w}{\dfrac{k_{fill}S_e}{2N_w}} \end{cases} \tag{4}$$

where N is the number of rotor poles of BSRM, $N = 8$; θ_{on} and θ_{off} are the off angle and on angle of the switch tube respectively; $\rho_{cu}(T_{cu})$, S_e, k_l, and k_{fill} are the conductivity of the winding, the cross-sectional area of the stator slot, the coefficient considering the end length, and the slot full rate. The calculation formula of the electric conductivity of the winding is:

$$\rho_{cu}\left(T_{cu}\right) = \rho_{cu0}\cdot\left[1+\alpha_{cu}\left(T_{cu}-T_0\right)\right] \tag{5}$$

where α_{cu}, T_{cu}, and T_0 are resistance temperature coefficient, winding temperature, and reference temperature.

In the process of motor operation, the additional loss mainly includes friction loss and ventilation loss. Due to the different doubly salient structures and rotating speeds of SRM, it is difficult to calculate the friction loss and ventilation loss with an accurate formula. In [16], mechanical loss and ventilation loss are considered as a whole and calculated. The calculation formula can be expressed as follows:

$$P_s = a_w V_{wl}\omega^{p_2} \tag{6}$$

where a_w is the wind resistance coefficient; V_{wl} is the volume of air inside the motor without considering the stator core; $P2$ is fitting coefficient.

Under the condition of high-speed operation, the iron loss increases exponentially, while HDSBSRM is a salient pole structure, so the analysis of iron loss will become very complicated. In [17], an improved separation model is proposed to separate the loss into hysteresis loss, classical eddy current loss, and abnormal loss. The calculation formula is as follows:

$$P_{Fe} = P_{hyst} + P_{eddy} + P_{exc} = k_{hyst} f B_m^2 + k_{eddy} f^2 B_m^2 + k_{exc} f^{1.5} B_m^{1.5} \tag{7}$$

where P_{hyst} is the hysteresis loss; P_{eddy} is the eddy current loss; P_{exc} is the abnormal loss; k_{hyst} is the coefficient of hysteresis loss; k_{eddy} is the eddy current loss coefficient; k_{exc} is the abnormal loss coefficient; f is the change frequency of magnetic induction intensity.

3.2. FEM Verification of Iron Loss

Iron loss result of HDSBSRM using finite element method at 10000 rpm is shown in Fig. 3. The figure shows the distribution diagram of the total iron loss of rotor at different mechanical angles. It can be seen that the bias magnetic field of permanent magnet produces eddy current loss on the rotor. When the rotor is in balance state, the control flux is 0, and only the permanent magnet bias flux produces the suspension force. However, when the rotor rotates, there are amplitude changes in the air gap magnetic density. The distribution of the rotor magnetic density is uneven, and the rotor magnetic field changes which causes iron loss.

The current of each phase and loss of HDSBSRM at 10000 rpm are shown in Fig. 4. The external circuit of the set motor is shown in Fig. 4(a), and the three-phase current waveform is shown in Fig. 4(b). Fig. 4(c) shows that the total hysteresis loss is about 20 W, and Fig. 4(d) shows that the eddy current

Table 2. Calculation results of iron loss.

Part	Outer stator	Inner stator	Rotor
Calculation (W)	90.8	2.1	49.2
FEM (W)	97.56	2.33	51.1

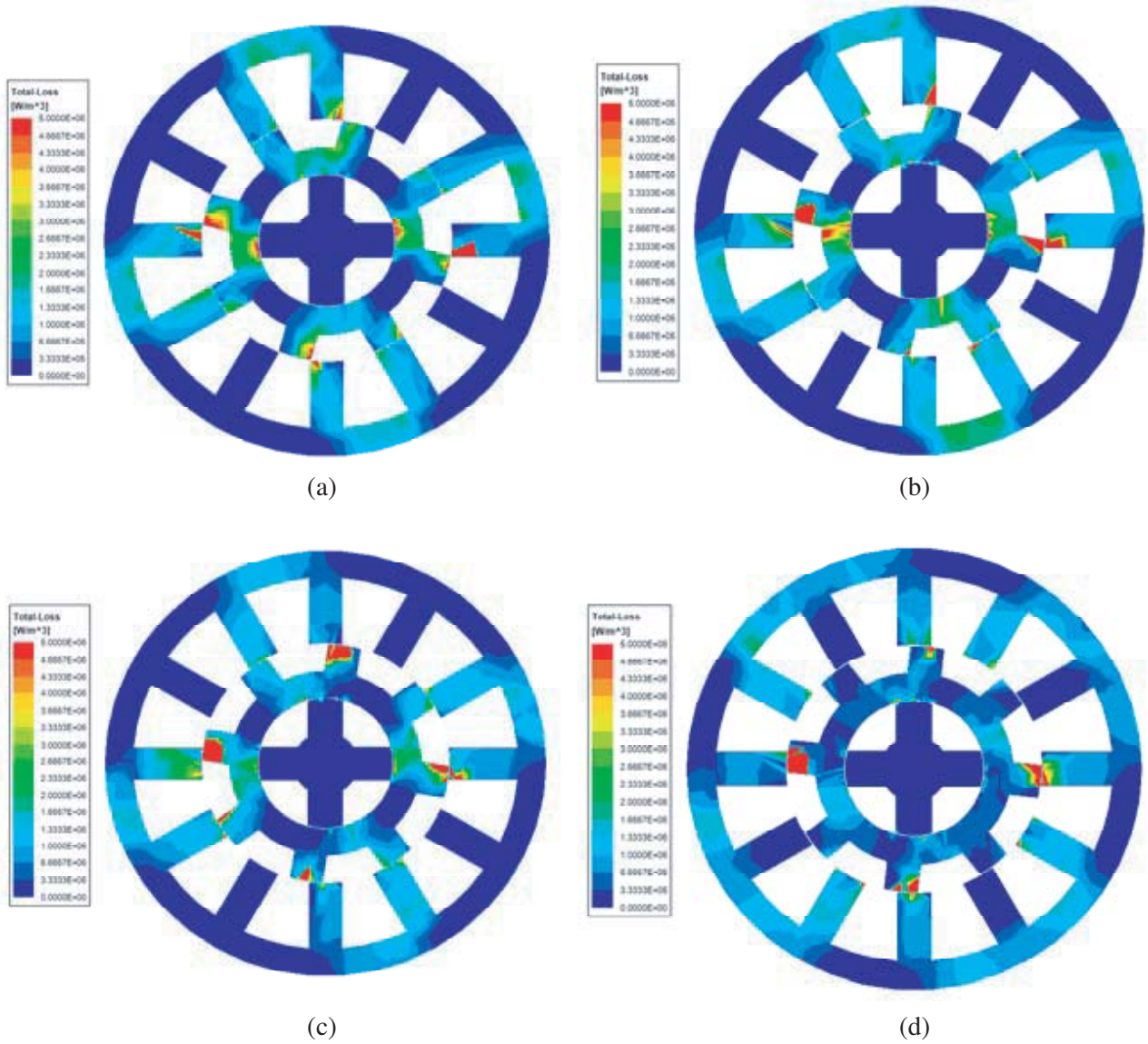

Figure 3. Finite element simulation diagram of iron loss. (a) $\theta = 0°$. (b) $\theta = 3°$. (c) $\theta = 6°$. (d) $\theta = 9°$.

loss of the motor is about 125 W. It can be concluded that the total iron loss of the motor is about 145 W.

Table 2 shows the motor loss results obtained by the calculation method and the finite element analysis method, respectively. It can be seen that the results of the two methods are similar.

4. ESTIMATE OF TEMPERATURE FIELD

The temperature field analysis in this paper is based on the 3D loss analysis model established by ANSYS. The loss data model is introduced into the Workbench. The loss is taken as the heat source, and the temperature rise curve of the motor is calculated by considering the structural differences and different heat conduction and heat dissipation coefficients of each part of the motor. Finally, the performance of the motor is analyzed.

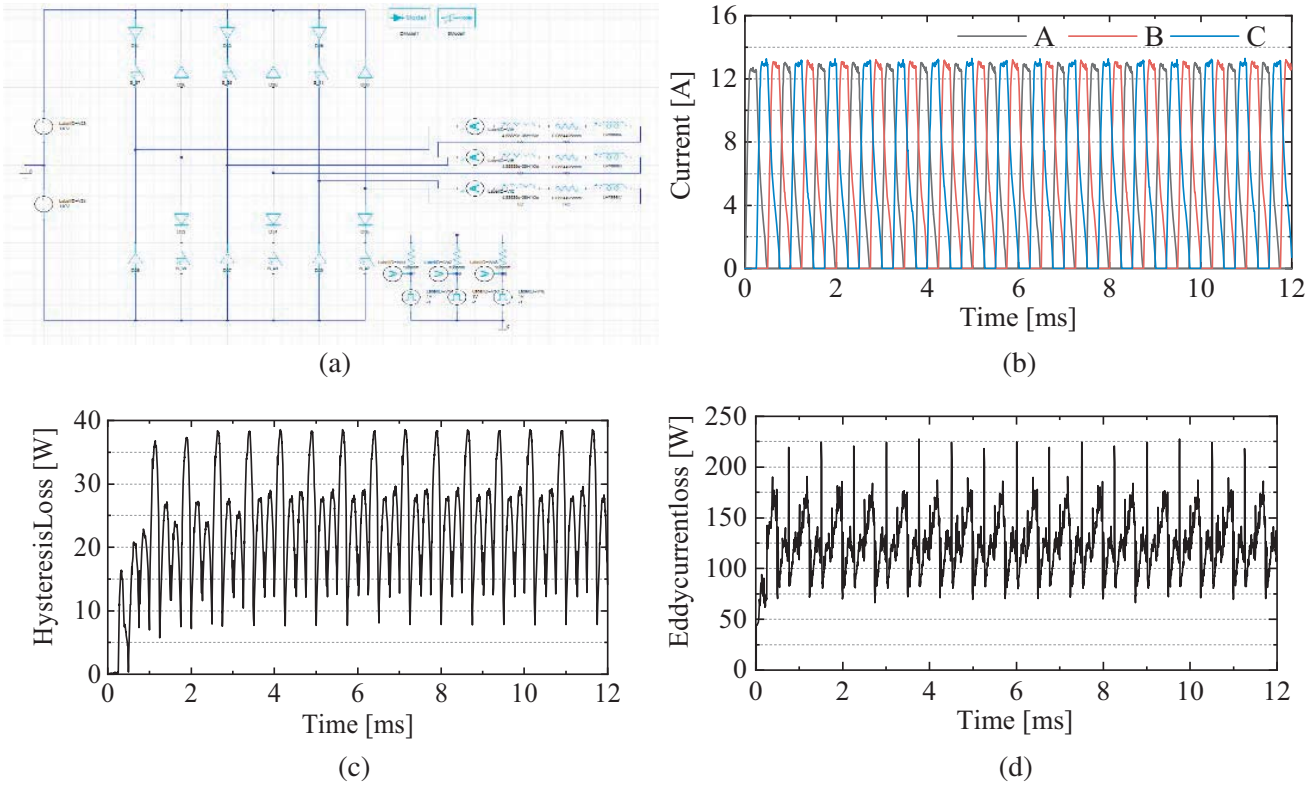

Figure 4. Loss with control current for HDSBSRM. (a) External circuit. (b) The three-phase current waveform. (c) Hysteresis loss. (d) Eddy current loss.

4.1. Thermal Model Parameters

4.1.1. Thermal Conductivity

The thermal conductivity of the main components of HDSBSRM mainly includes the thermal conductivity of winding, air gap, and stator/rotor core. It is relatively difficult to accurately model the equivalent insulator of the motor winding. Therefore, the simplified modeling of the motor winding is carried out. The calculation formula of the equivalent insulator thermal conductivity of the winding is as follows:

$$\lambda_{eq} = \sum_{n=1}^{n} \delta_i \Big/ \sum_{n=1}^{n} \frac{\delta_i}{\lambda_i} \tag{8}$$

where λ_{eq} is the thermal conductivity of the equivalent insulator of the winding; δ_i and λ_i are the thickness and thermal conductivity of each layer of insulator.

The stator core is made of a silicon steel sheet, which is equivalent to the heat transfer between two steel plates. Therefore, the calculation formula of the equivalent thermal conductivity is as follows:

$$k = \frac{x_a + x_b}{x_a/k_a + x_a/k_b} \tag{9}$$

where x_a is the thickness of the first steel plate; x_b is the thickness of the second steel plate; k_a is the thermal conductivity of the first steel plate; k_b is the thickness of the second steel plate.

The air in the air gap is statically treated, and the equivalent thermal conductivity of the air gap is described by the thermal conductivity of the static air [18]:

$$\lambda_{eff} = 0.23\beta \left(\frac{\delta}{R_r}\right)^{0.25} Re^{0.5}\lambda_k \tag{10}$$

where β is the empirical coefficient of the rotor surface; R_r is the outer diameter of the rotor; λ_k is the thermal conductivity of air in the air gap; δ is the air gap length; Re is the Reynolds coefficient. The calculation formula is:

$$Re = \frac{\omega_r}{v_0} \tag{11}$$

where ω_r is the rotor angular speed; v_0 is the kinematic viscosity of air in the air gap.

Table 3 shows the values of heat conduction parameters of motor materials during thermal analysis.

Table 3. Heat conduction parameters of each material.

Part	Material	Density (kg/m^3)	Specific Heat Capacity ($J/kg \cdot K$)	Thermal Conductivity ($W/(m \cdot K)$)
Outer Stator	DW470	7800	450	70
Inner Stator and rotor	Pure iron	7897	452	67.5
Slot insulation	Composite	1.2	1340	0.3
Winding	Copper	8900	390	386
Air gap (10000 rpm)	Air	1.29	1004	0.13
Permanent magnet	NdFe35	8300	544	11

4.1.2. Internal Heat Generation Rate

The temperature rise of the motor is caused by various losses inside the motor. The losses calculated by the finite element analysis are loaded into the thermal model as a heat source. However, due to the inaccuracy of the calculation results of copper loss in the finite element simulation results, the formula method is used separately to calculate the heat generation rate of the motor winding, and the calculation formula of the heat generation rate of the winding is as follows:

$$q = \rho \cdot J^2 \tag{12}$$

where ρ is the resistivity; J is the current density.

4.1.3. Surface Convective Heat Transfer Coefficient

The convective heat transfer coefficient between the shell and the air is:

$$\alpha_m = 14\left(1 + 0.5\sqrt{\omega}\right)^3 \sqrt{\frac{T_0}{25}} \tag{13}$$

where ω is the internal wind speed of the casing; T_0 is the ambient temperature.

The heat dissipation coefficient of winding and stator end face is:

$$\alpha_w = \alpha_s = \frac{1 + 0.04\omega_r}{0.045} \tag{14}$$

where ω_r is the outer diameter linear speed of the rotor.

The convective heat transfer coefficient of rotor end face is:

$$\alpha_r = 28\left(1 + \sqrt{0.45\omega_r}\right) \tag{15}$$

4.1.4. Model of Temperature Field

The three-dimensional model of the motor is imported into ANSYS/Workbench, and the finite element model of transient temperature field is established. The heat conduction model of the motor, the heat generation rate of the heating part, and the convection heat dissipation coefficient of the convection surface are set in the model. Secondly, in order to make the model more accurate, the winding and the equivalent insulation need to be subdivided. The three-dimensional model of the motor is shown in Fig. 5.

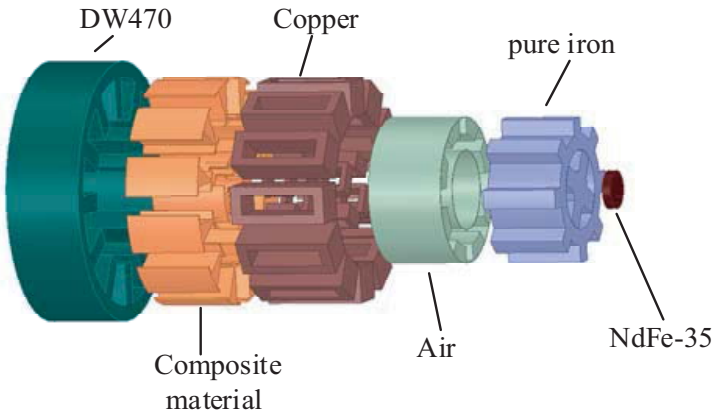

Figure 5. 3D thermal model.

4.2. Temperature Field Simulation Results and Analysis

The temperature field analysis of the motor is shown in Fig. 6. Figs. 6(a) and 6(b) are the heat flux diagrams from different perspectives, from which we can know the heat dissipation direction and speed of each part of the motor, of which the heat dissipation rate of the rotor end face is the largest.

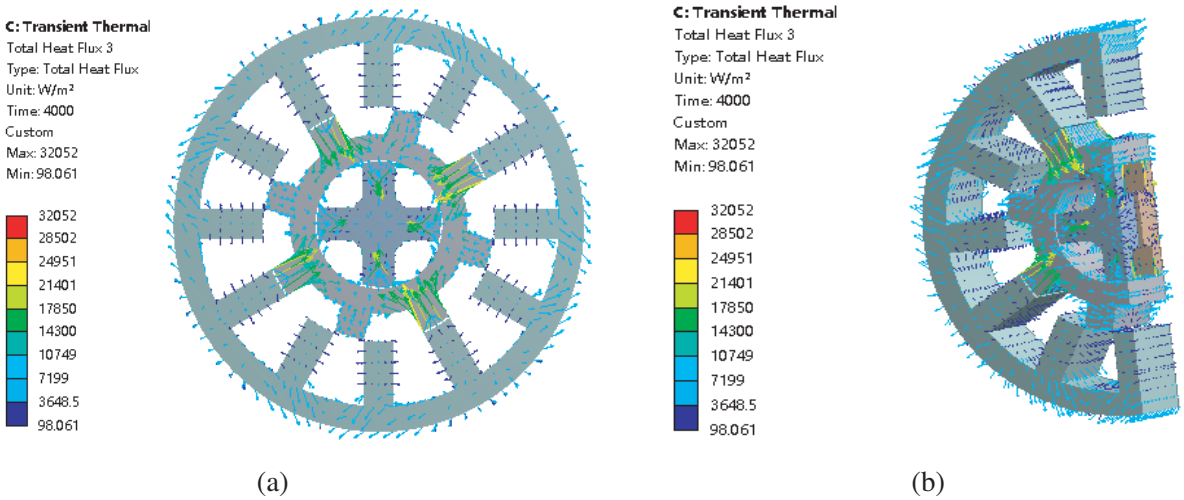

Figure 6. Heat flux diagram. (a) Front view. (b) Side view.

Figures 7(a)–7(e) show the temperature distribution of each part of the motor. From the figure, it can be seen that the maximum temperature rise of the motor is 89.75°, and the overall temperature is high, but within the controllable range. Because of the low loss of the innerstator, its temperature is relatively low. Due to the high heat dissipation rate at the end, the temperature at the axial middle position of the motor is higher, and the temperature at both ends is lower. However, the temperature of the rotor teeth is lower, and the temperature of the yoke is higher, which is consistent with the loss analysis results.

In order to see the temperature rise of each part of the motor more intuitively, Fig. 8 shows the temperature rise curve of the main structure of the motor, including the double stator, rotor, and winding. It can be clearly seen that the temperature of the motor has reached steady state within 4000 s. The temperature rise of outer stator and winding is the highest, and that of inner stator is the lowest, which is consistent with the loss analysis.

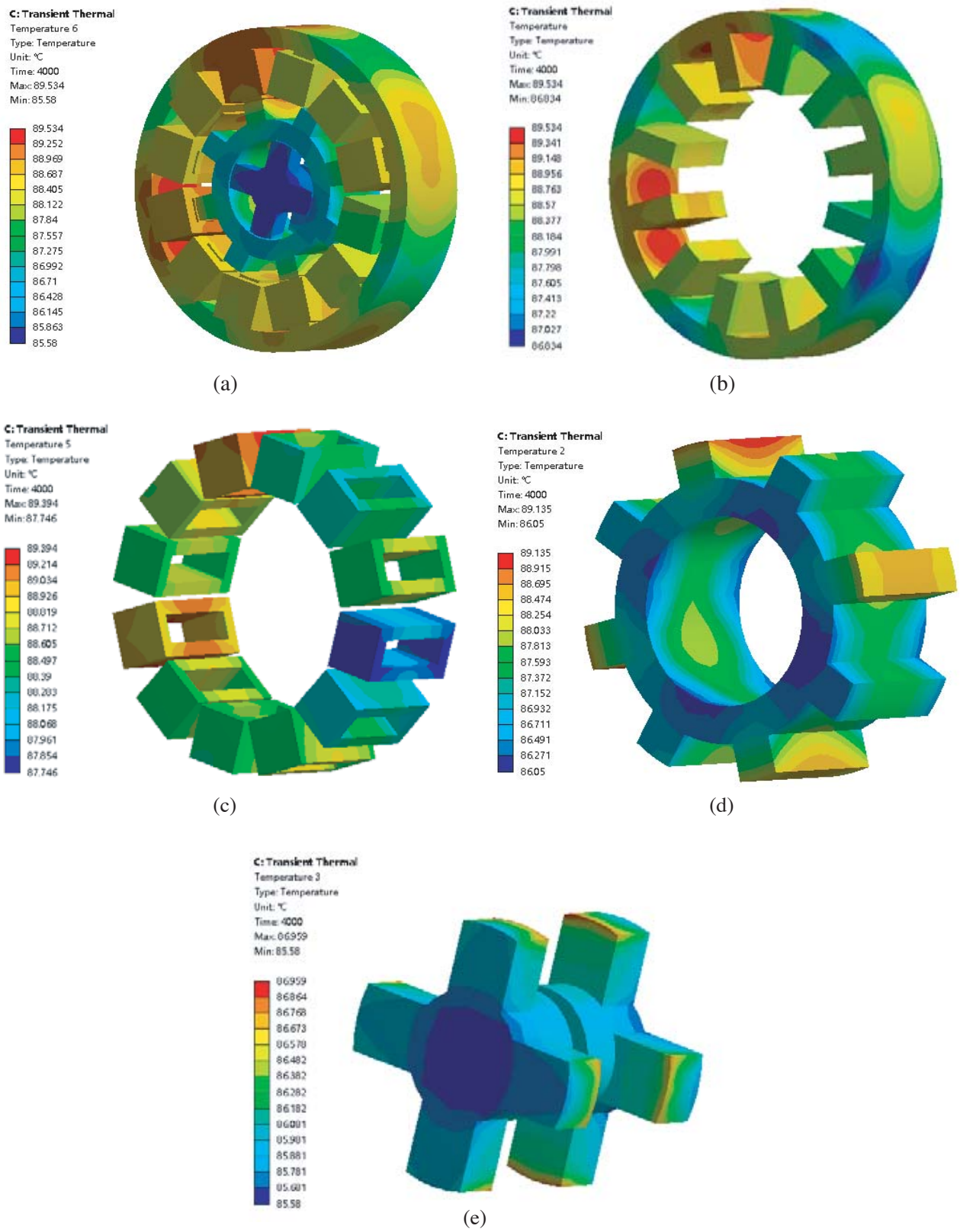

Figure 7. Analysis results of temperature field. (a) Overall. (b) Outer stator. (c) Winding. (d) Rotor. (e) Inner stator.

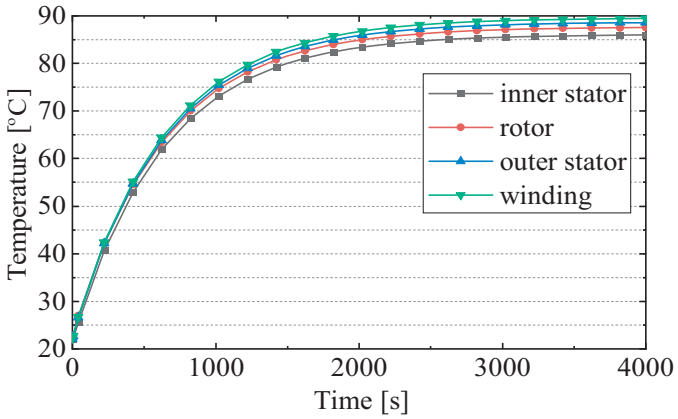

Figure 8. Temperature rise curve.

5. CONCLUSION

Based on the introduction of the internal structure of a 12/8/4 HDSBSRM, the loss of the motor is analyzed and calculated by the formula method and finite element method, respectively. On this basis, the three-dimensional loss model of the motor is imported into the Workbench software to analyze the temperature rise characteristics of the motor. The results show that the value of loss and temperature rise analysis results of the HDSBSRM motor are basically consistent with the pre estimate. At high speed, the temperature of motor rises rapidly, and the final temperature of winding, rotor tooth, and stator tooth is relatively high. Therefore, in the design of a bearingless motor, in order to reduce the temperature rise, it is necessary to reduce the loss of the motor in the premise of ensuring the electromagnetic performance of the motor. This study provides a basis for the performance verification and optimal design of the motor.

ACKNOWLEDGMENT

This work was sponsored by the National Natural Science Foundation of China (51707082, 51877101), Open Research Fund of Jiangsu Collaborative Innovation Center for Smart Distribution Network, Nanjing Institute of Technology (No. XTCX202009) and Priority Academic Program Development of Jiangsu Higher Education Institutions (No. PAPD-2018-87).

REFERENCES

1. Ahmed, F., K. Kalita, and H. B. Nemade, "Torque and controllable radial force production in a single winding bearingless switched reluctance motor with a speed controlled drive operation," *International Transactions on Electrical Energy Systems*, Vol. 30, No. 5, 2020.
2. Takemoto, M., A. Chiba, and T. Fukao, "A new control method of bearingless switched reluctance motors using square-wave currents," *Power Engineering Society Winter Meeting*, 375–380, Singapore, 2000.
3. Chen, L. and W. Hofmann, "Design procedure of bearingless high-speed switched reluctance motors," *International Symposium on Power Electronics, Electrical Drives Automation and Motion*, 1442–1447, 2010.
4. Zhou, Y., Y. Sun, X. Ji, et al., "A novel bearingless switched reluctance generator," *Proceedings of the CSEE*, Vol. 32, No. 15, 107–113, 2012.
5. Sun, Y., F. Yu, Y. Yuan, et al., "A hybrid double stator bearingless switched reluctance motor," *Diangong Jishu Xuebao/Transactions of China Electrotechnical Society*, Vol. 34, No. 1, 1–10, 2019.

6. Yuan, Y., Y. Ma, S. Guo, F. Yang, and B. Xu, "Suspension performance analysis of a novel bearingless motor," *Electronics Letters*, Vol. 56, No. 3, 132–134, 2020.
7. Zhao, B., *Application of Ansoft 12 in Engineering Electromagnetic Field*, Water Power Press, Beijing, China, 2010 (in Chinese).
8. Yuan, Y., Y. Sun, and Y. Huang, "Accurate mathematical model of bearingless flywheel motor based on Maxwell tensor method," *Electronics Letters*, Vol. 52, No. 11, 950–951, 2016.
9. Wang, T., X. Ouyang, L. Li, and X. Li, "Optimization of the five phase fault tolerant motor based on Ansoft simulation," *IEEE/CSAA International Conference on Aircraft Utility Systems (AUS)*, 1035–1039, Beijing, China, Oct. 2016.
10. Yuan, Y., Y. Sun, and Y. Huang, "Design and analysis of bearingless flywheel motor specially for flywheel energy storage," *Electronics Letters*, Vol. 52, No. 1, 66–68, 2016.
11. Liu, J., X. Zhang, H. Wang, et al., "Iron loss characteristic for the novel bearingless switched reluctance motor," *2013 International Conference on Electrical Machines and Systems (ICEMS)*, 586–591, IEEE, 2013.
12. Liu, Z., S. Wang, and Z. Deng, "Inductance characteristics for bearingless switched reluctance motors under condition of steady magnetic suspension," *Journal of Nanjing University of Aeronautics & Astronautics*, Vol. 41, No. 2, 165–170, 2009.
13. Liu, C., X. Zhu, Y. Du, et al., "Design and performance analysis of magnetic field modulated flux-switching permanent magnet machine based on electrical-thermal bi-directional coupling design method," *Proceedings of the CSEE*, Vol. 37, No. 21, 6237–6245, 2017.
14. Howey, B., E. Rowan, B. Bilgin, et al., "Thermal trade-off analysis of an exterior rotor e-bike switched reluctance motor," *IEEE Transportation Electrification Conference and Expo (ITEC)*, 605–612, 2017.
15. Qi, J., W. Hua, and H. Zhang, "Thermal analysis of modular-spoke-type permanent-magnet machines based on thermal network and FEA method," *IEEE Transactions on Magnetics*, Vol. 55, No. 7, 1–5, 2019.
16. Zhu, L., J. Shen, X. Gong, L. Liu, J. Liu, and Z. Xu, "Effects of different modes of mechanical ventilation on aerodynamics of the patient-specific airway: A numerical study," *2019 41st Annual International Conference of the IEEE Engineering in Medicine and Biology Society (EMBC)*, 4961–4964, Berlin, Germany, 2019.
17. Bertotti, G., "Physical interpretation of eddy current losses in ferromagnetic materials. I. Theoretical considerations," *Journal of Applied Physics*, Vol. 57, No. 6, 2110–2117, 1985.
18. Howey, D. A., P. R. N. Childs, and A. S. Holmes, "Air-gap convection in rotating electrical machines," *IEEE Transactions on Industrial Electronics*, Vol. 59, No. 3, 1367–1375, 2012.